

## Re-examination of the I-5 dust storm

Michael L. Kaplan,<sup>1</sup> Ramesh K. Vellore,<sup>2</sup> John M. Lewis,<sup>3,1</sup> S. Jeffrey Underwood,<sup>4</sup> Patricia M. Pauley,<sup>5</sup> Jonathan E. Martin,<sup>6</sup> and R. Krishnan<sup>2</sup>

Received 23 October 2012; revised 30 November 2012; accepted 20 December 2012; published 31 January 2013.

[1] The infamous dust storm over the thanksgiving holiday of 1991 that led to loss of life from numerous automobile accidents on Interstate 5 (I-5) has been re-examined. Pauley *et al.* (1996) conducted an earlier investigation of this dust storm following the tenets of Danielsen's paradigm—a paradigm that links the tropopause fold phenomenon and a balanced thermally indirect circulation about the upper level jet stream. However, a cursory examination of mesoscale structures in the storm from the North American Regional Reanalysis (NARR) indicated evidence of a low-level unbalanced thermally direct circulation that demanded further investigation using a high-resolution Weather Research and Forecasting (WRF) model simulation. Principal results from the present study follow: (1) Although the model simulation showed evidence of a weak indirect circulation in the upper troposphere in support of the Danielsen's paradigm, the dynamic control of the storm stemmed from the lower tropospheric mesoscale response to geostrophic imbalance. (2) A lower tropospheric direct circulation led to mass/temperature adjustments that were confirmed by upper air observations at locations in proximity to the accident site, and (3) boundary layer deepening and destabilization due to these mesoscale processes pinpointed the timing and location of the dust storm. Although the present study does not underestimate the value of analyses that focus on the larger/synoptic scales of motion, it does bring to light the value of investigation that makes use of the mesoscale resources in order to clarify synoptic-mesoscale interactions.

**Citation:** Kaplan, M. L., R. K. Vellore, J. M. Lewis, S. J. Underwood, P. M. Pauley, J. E. Martin, and R. Krishnan (2013), Re-examination of the I-5 dust storm, *J. Geophys. Res. Atmos.*, 118, 627–642, doi:10.1002/jgrd.50131.

### 1. Introduction

[2] Following the investigation of dust storms over the Black Rock Desert (BRD) and more generally north-central Nevada [Lewis *et al.*, 2011; Kaplan *et al.*, 2011—subsequently referred to as BRD studies], a view of dust storm generation was developed that differed from the classic view of Danielsen [Danielsen, 1968, 1974; Pauley *et al.*, 1996; Martin, 2008; Schultz and Meissner, 2009]. Succinctly stated, the Danielsen view places emphasis on elongated trajectories that originate in the lower stratosphere and descend into the troposphere with speeds on the order of 30–40 m s<sup>-1</sup> (the “tropopause fold”

phenomenon). Upon reaching the low-level adiabatic layer that typically resides over the deserts of the western USA in late spring, summer, and early fall, momentum rapidly mixes to the ground as strong wind gusts. The underlying dynamics are quasi-geostrophic (Q-G) where an indirect transverse circulation about the jet leads to descending motion on the right side (anti-cyclonic/warm-air side). Danielsen's exquisite manual upper air analyses were based on the assumption of isentropic flow where data came from rawinsondes and instrumented aircraft (in some cases). In the BRD studies mentioned above, the mechanism for dust storm generation is linked to geostrophic adjustment—an initial large-scale geostrophic imbalance primarily rectified by a sub-synoptic mass-field adjustment where direct transverse circulations about the jet lead to the generation of low-level ageostrophic/isallobaric winds [Rochette and Market, 2006] that ablate dust in the well-mixed turbulent boundary layer.

[3] In the presence of results from the BRD studies, a cursory retrospective examination of atmospheric conditions surrounding the dust storm of November 1991 was undertaken. Pauley *et al.* [1996] performed the initial study of this dust storm. The storm occurred in the San Joaquin Valley of California (Figure 1) at 2200 UTC 29 November 1991; the large volume of traffic over the thanksgiving holiday led a series of automobile accidents and loss of life [Covitz *et al.*, 1992].

[4] Arguments in Pauley *et al.* [1996] followed the Danielsen paradigm [Danielsen, 1974] to a large degree.

<sup>1</sup>Division of Atmospheric Sciences, Desert Research Institute, Reno, Nevada, USA.

<sup>2</sup>Centre for Climate Change Research, Indian Institute of Tropical Meteorology, Pune, India.

<sup>3</sup>National Severe Storms Laboratory, Norman, Oklahoma, USA.

<sup>4</sup>Department of Geology and Geography, Georgia Southern University, Statesboro, Georgia, USA.

<sup>5</sup>Marine Meteorology Division, Naval Research Laboratory, Monterey, California, USA.

<sup>6</sup>Department of Atmospheric and Oceanic Sciences, University of Wisconsin, Madison, Wisconsin, USA.

Corresponding author: Dr. M. L. Kaplan, Desert Research Institute, 2215 Raggio Parkway, Reno, NV 89512, USA. (Mike.Kaplan@dri.edu)

©2013. American Geophysical Union. All Rights Reserved.  
2169-897X/13/10.1002/jgrd.50131

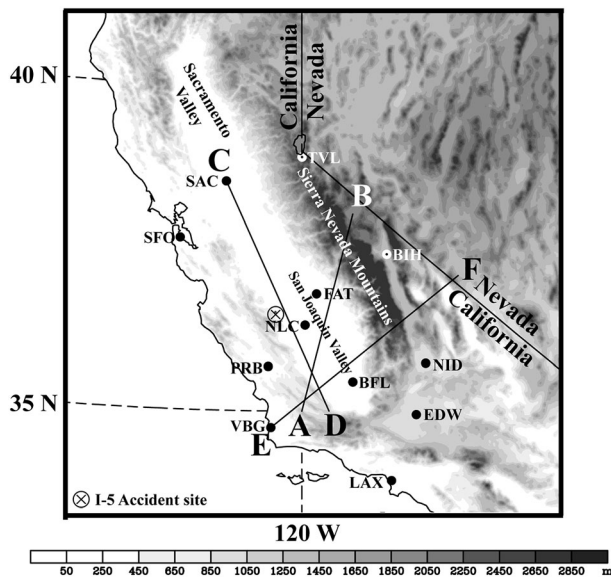


**Figure 1.** Topographical map of California and Nevada (Source: United States Geological Survey). Also shown are station locations with identifiers and the Great Central Valley in California where its northern (southern) half is referred to as the Sacramento (San Joaquin) Valley, Sierra Nevada Mountains, and the vertical cross sections (A-B, C-D, and E-F) used in the study. The accident site is marked by  $\otimes$ .

The vertical motions were found by examination of analyses from the U. S. Navy's optimum interpolation data assimilation scheme [Barker, 1992] where the forecast from the Navy's operational regional prediction model served as the background (NORAPS: Navy Operational Regional Atmospheric Prediction System) [Liou *et al.*, 1994; Hodur, 1987]. The synoptic analyses (grid resolution of 60 km) at 700 hPa (cf. Figures 14 and 15 from Pauley *et al.* [1996]) gave evidence of an indirect circulation about the jet just north of the accident location (indicated by  $\otimes$  in Figure 1) at the time of the accident. With the advantage of the more recent NARR (North American Regional Reanalysis) [Mesinger *et al.*, 2006] data set with a finer resolution of 32 km and background fields from the Eta model, the corresponding vertical motion pattern from NARR gives evidence of a smaller-scale ascent at the time and place of the accident—indicative of a sub-synoptic scale direct circulation in agreement with the BRD studies.

[5] The scientific justification for this research lies to a large extent in the fact that these preliminary findings strongly underscore how mesoscale jet streak adjustment processes, even in the absence of strong diabatic heating, may control low-level mass and momentum fields. In particular, the preliminary findings highlight how thermally direct and unbalanced ageostrophic circulations at the mesoscale within the lower troposphere can supercede larger-scale balanced circulations in terms of changing the low-level mass and momentum fields. Dust storms are tracers for these turbulence kinetic energy (TKE)-generating processes. These adjustments are finer in scale than quasi-geostrophic adjustments but larger in scale than most convective cells and convective clusters; thus, they exist in a space/time scale

not always well observed and ubiquitously referenced as causing important mesoscale weather phenomena.

[6] Without refuting the existence of a large-scale indirect circulation, yet in the presence of some evidence of a direct circulation on a smaller scale, a decision was made to more carefully examine the I-5 dust storm with the advantage of the Weather Research and Forecasting (WRF) model [Skamarock *et al.*, 2008] that was used in the second of the BRD studies mentioned earlier [Kaplan *et al.*, 2011].

[7] We begin our study with an examination of the synoptic and sub-synoptic flow fields prior to the development of the I-5 dust storm. An outline of the numerical experiment design follows, along with a synthesis of the results. We conclude with a discussion of processes that govern the generation of the dust storm.

## 2. Setup for the I-5 Storm

[8] To clarify critically important synoptic and mesoscale structures that set the stage for the storm, our examination is divided into a pre-storm synoptic scale period from 1200 UTC 28 November 1991 to 1200 UTC 29 November 1991 (labeled “day 1”) and the immediate mesoscale period from 1500 UTC 29 November 1991 to 2100 UTC 29 November 1991 (labeled “day 2”). The NARR products, manually constructed surface analyses, and a Landsat geomorphology product are used in this examination.

### 2.1. Day 1—Synoptic Setup: 1200 UTC 28 November 1991–1200 UTC 29 November 1991

[9] Figure 2 shows the 500 hPa geopotential height, horizontal winds, and temperature fields at 1200 UTC 28 November 1991 and 0000 UTC 29 November 1991, and Figure 3 shows the 700 hPa vertical motions at 1800 UTC 28 November 1991 from NARR, respectively. A deep cold positively tilted (northeast-southwest orientation) trough is centered over an area extending from Montana down through southern California and west of Baja California at 1200 UTC 28 November 1991. It moves eastward and slightly southward over the subsequent 12 h period. Another strong baroclinic zone is noted over British Columbia in Canada at 1200 UTC 28 November 1991 with a low-amplitude geopotential ridge that is oriented along a line that passes through Washington-Oregon-Idaho (indicated in Figure 2). This baroclinic zone intensifies and advances southward into the Pacific Northwest by 0000 UTC 29 November 1991.

[10] A classic ascent/descent pattern is apparent from the 700 hPa vertical motion fields at 1800 UTC 28 November 1991 with descending pattern behind the trough over most of California (shown in Figure 3) and ascending pattern over eastern Arizona (not shown) ahead of the trough. Further, there is evidence of a Q-G indirect circulation in the exit region of the jet—a circulation that runs across the section from northeast Arizona through southern California. Also apparent is a strong northeast-southwest mesoscale gradient of lifting indicative of a possible mountain wave structure extending from the Central Valley of California (Figure 1) northeastwards to the crest of the Sierra Nevada Mountains. Air from above 700 hPa is being forced down the Sierra Nevada and adiabatically warmed by the cross-mountain (north-northeasterly) flow at 1800 UTC 28 November 1991 accompanying the jet streak.

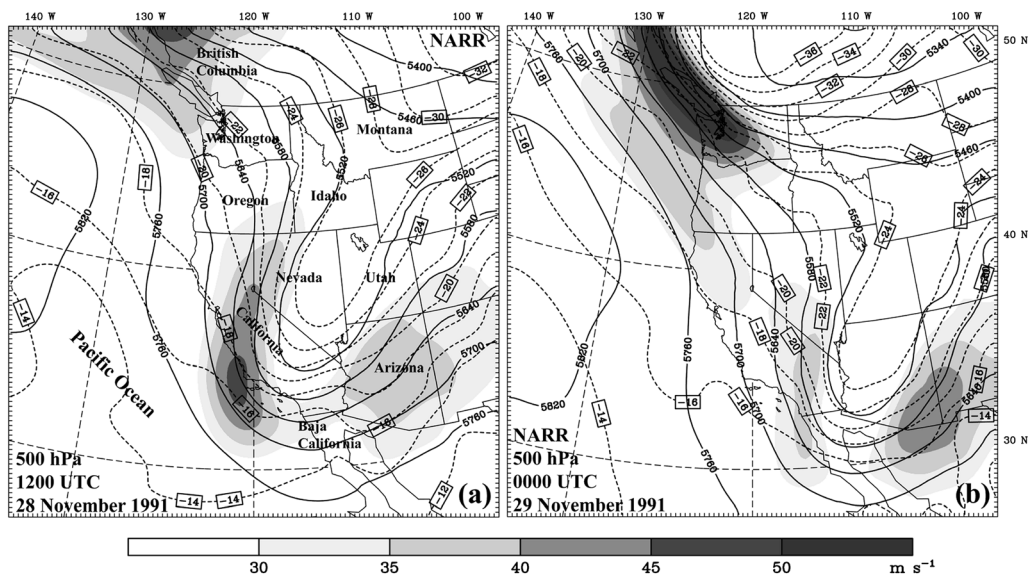


**Figure 2.** The 500 hPa horizontal winds (gray shaded; isotachs;  $\text{m s}^{-1}$ ), geopotential height (solid; contour interval = 60 m), and air temperature (dashed; contour interval =  $2^\circ\text{C}$ ) from NARR at (a) 1200 UTC 28 November 1991 and (b) 0000 UTC 29 November 1991. State identifiers (California, Montana, Oregon, Nevada, Utah, and Oregon from the U.S.; British Columbia from Canada; and Baja California from Mexico) used in the study are shown in the figure.

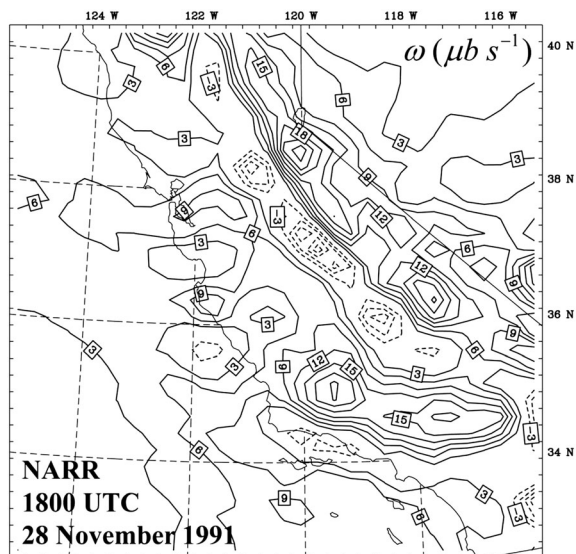


**Figure 3.** The 700 hPa vertical p-velocity (contour interval =  $3 \mu\text{b s}^{-1}$ ) from NARR at 1800 UTC 28 November 1991.

[11] Figure 4 shows the 750 hPa air temperature at 0900 and 1500 UTC 29 November 1991. This clearly exhibits the warming over California and the adjoining region over the Pacific Ocean. The strong temperature gradient over most of California reflects the aforementioned vertical circulations. Two baroclinic zones are apparent: (1) a meso- $\alpha$  scale (approximately 750 km) zone-oriented south-north and located within the warm Laplacian of temperature over the northern California coast and a west-east-oriented meso- $\beta$  scale zone (approximately 100 km) closely aligned with the lee (western) side of the Sierra Nevada Mountains (Figure 1), i.e., from Central California northeastwards.

The meso- $\alpha$  scale (200–2000 km) and meso- $\beta$  scale (20–200 km) definitions are derived from *Orlanski* [1975]. These baroclinic zones below the 700 hPa descending air (Figure 3) reflect the meso- $\alpha$  scale jet exit region indirect circulation and meso- $\beta$  scale sinking imposed by orographic descent on the western side of the Sierra Nevada accompanying cross-mountain north-northeasterly airflow.

[12] The adiabatic warming signal gives rise to a large-magnitude lower tropospheric geopotential height gradient and associated large-magnitude veering geostrophic flow above the western (lee) side of the Sierra Nevada (vertical sounding not shown). This veering geostrophic flow is not in thermal wind balance ahead of the second (upstream) jet streak that arrives just 3–6 h after 0900 UTC 29 November 1991. The second lower mid-tropospheric jet streak associated with the baroclinic zone over the Pacific Northwest advances into this pre-conditioned mass field with multiple baroclinic zones which leads to a severe geostrophic imbalance—a sub-geostrophic flow regime accompanying thermal wind imbalance signature found in the BRD studies mentioned in the introduction.

## 2.2. Day 2—Mesoscale Structure: 1500–2100 UTC 29 November 1991

[13] Figures 4–6 show the 1500 UTC 750 hPa temperature, horizontal winds on the 299 K isentropic surface, and vertical motions on the 800 hPa surface from NARR during 1500–1800 UTC 29 November 1991, respectively. Clearly, the jet streak over British Columbia that was evident at 1200 UTC 28 November 1991 (Figure 2) has advanced into California at these later times with a noticeable development of curvature in the region of maximum winds. This development is evidence of a mesoscale adjustment to the sub-geostrophic flow regime that was a hallmark of the earlier BRD studies, i.e., lifting, adiabatic cooling, and height falls.

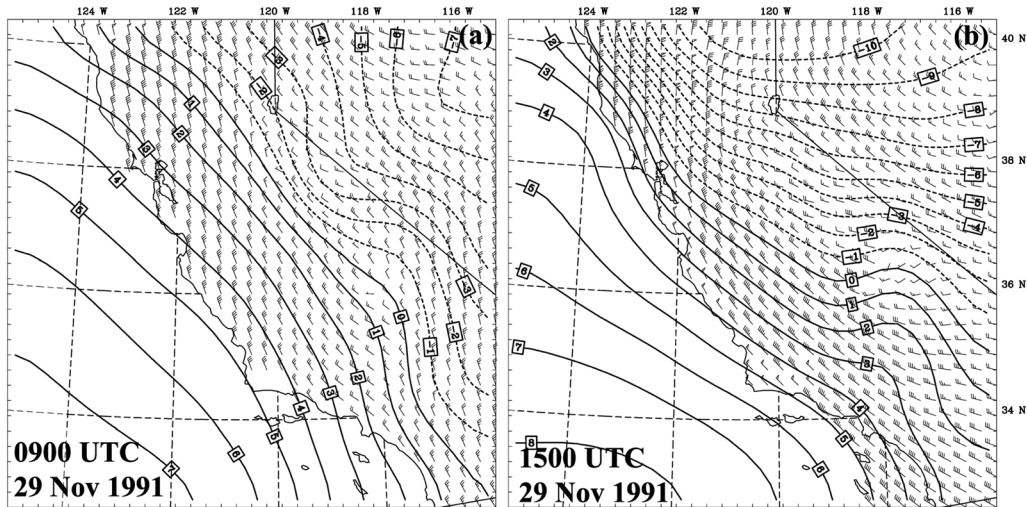


**Figure 4.** The 750 hPa air temperature (contour interval = 1°C) and horizontal winds (full barb = 5 m s<sup>-1</sup>) from NARR at (a) 0900 UTC and (b) 1500 UTC 29 November 1991.

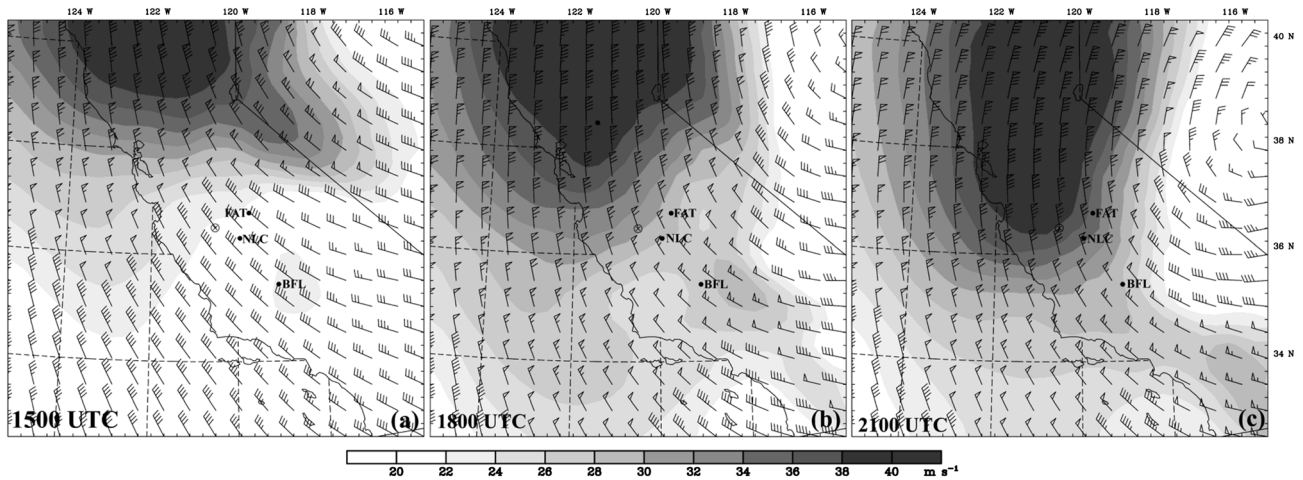


**Figure 5.** Horizontal winds (full barb = 5 m s<sup>-1</sup>) on the 299 K isentropic surface [isotachs shaded (m s<sup>-1</sup>)] from NARR at (a) 1500 UTC, (b) 1800 UTC, and (c) 2100 UTC 29 November 1991. The accident site is marked by ⊗.

The net effect of these adjustments is cold air development, and its movement across the jet from east to west toward the Central Valley of California can be seen in Figure 4b.

[14] Consistent with this cooling and height falls is a mesoscale wind maximum (jetlet) in the left exit region of the geostrophic jet streak which can be seen to develop by 1500 UTC 29 November 1991 over south central California just southeast of Bakersfield (BFL) and to strengthen/propagate slowly southeastwards through 2100 UTC to the south of Edwards Air Force Base (EDW). This signal of accelerating flow, approximately 8 m s<sup>-1</sup> in 3 h during 1500–1800 UTC 29 November 1991, in the exit region southeast of BFL (Figures 5a and 5b) organizes velocity divergence and an ascending motion maximum (Figure 6). This ascending maximum propagates rapidly southwards from south of NLC to southwest of EDW during the 1500–2100 UTC period.

[15] The mesoscale ascent, located between the larger jet streak’s exit region and the entrance region of the jetlet, strengthens exceeding 20 μb s<sup>-1</sup> by 2100 UTC 29 November 1991. This ascent feature differentiates the predominantly Q-G descent/ascent pattern behind and ahead of the trough in the NORAPS 700 hPa vertical motion ( $\omega$ ) field from a mesoscale ascent zone just north of the jetlet in the NARR 700 hPa  $\omega$ -field seen at 1800 UTC 29 November 1991 shown in Figure 7 in the region surrounding the stations BFL-Lemoore NAS (NLC)-Paso Robles (PRB) [see Figure 1 for station locations]. Note that the NARR displayed ascending motions in the southern part of the Central Valley of California as compared to the virtually nonexistent ascending motions in the NORAPS analysis at the same time and location. However, the ascent displayed by the NARR is inconsistent with Q-G theory descent behind the trough.

[16] The strong 700–800 hPa ascent through central and southern California is responsible in large part for the cooling mentioned above—an adiabatic cooling in response to this non Q-G ascent followed by subsequent south-southwestward horizontal advection of cold air. The frontal passage caused by this non-uniform mesoscale cold air advection produces the rapid temperature fall beneath 600 hPa observed in the Vandenberg Air Force Base (VGB) radiosonde observations at 0000 UTC 30 November 1991 (see also Figure 19b). This rapid cooling occurs at VGB in only 3 h in both the NARR as well as WRF simulation which will be discussed later.

[17] The NARR mean sea level pressure ( $P_{MSL}$ ) and horizontal winds at 975 hPa at 1800 and 2100 UTC 29 November 1991 are shown in Figure 8. The mesoscale depletion of mass in the columns of ascending air gives rise to the low pressure pattern (and associated inverted trough) that propagates southward while simultaneously extending northwestward in the Central Valley of California (Figure 1). This mesoscale inverted trough is upstream of the synoptic-scale low-pressure center over extreme southeastern California. This is occurring under the aforementioned jetlet on the 299 K isentropic surface with associated lifting and adiabatic cooling.

[18] Manual subjective surface pressure analyses shown in Figure 9 further add detail to the NARR products. Notice that the subjectively analyzed inverted trough of low pressure has a more west-east orientation than the pattern displayed by NARR. Further, it exhibits much smaller-scale contraction from meso- $\alpha$  scale in NARR to meso- $\beta$  scale in the analyzed surface observations. In view of the pressure tendency field shown in Figure 10, it is apparent that a major component of the surface winds is an ageostrophic/isallobaric flow.

[19] The isallobaric part ( $\vec{V}_{is}$ ) of the ageostrophic wind ( $\vec{V}_{ag}$ ) [Bluestein, 1992; Martin, 2006; Rochette and Market, 2006] is given as follows:

$$\vec{V}_{is} = -\frac{1}{\rho f^2} \nabla_z \left( \frac{\partial P_{MSL}}{\partial t} \right) \quad (1)$$

where  $\rho$  is the air density and  $f$  is the Coriolis parameter. This component is caused by air accelerating into the meso- $\beta$  scale trough across the southern part of the San Joaquin Valley (Figure 1). The structure of the lower level tropospheric fields and surface pressure patterns (Figures 8–10) give evidence of mesoscale mass-field adjustment in response to the large-scale geostrophic imbalance. This combination of features was found and addressed in the BRD studies.

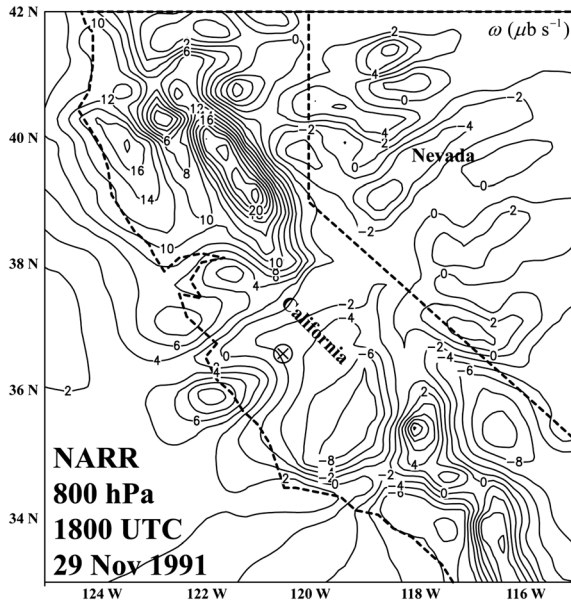


**Figure 6.** The 800 hPa vertical motion (contour interval =  $2 \mu\text{b s}^{-1}$ ) from NARR at 1800 UTC 29 November 1991 (Source: <http://nomads.ncdc.noaa.gov>; Rutledge et al. [2006]). Thick dotted lines show the state boundaries for California and Nevada. The accident site is marked by  $\otimes$ .

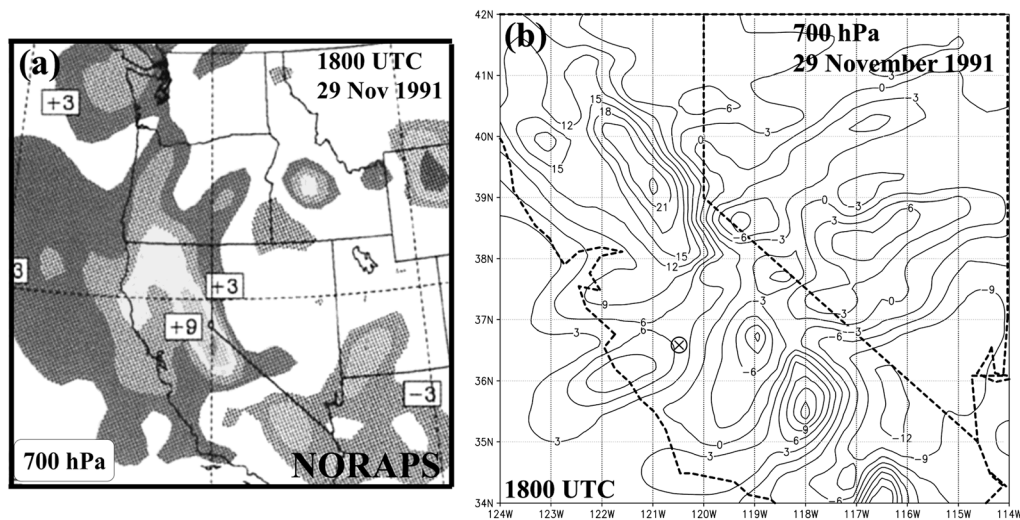


**Figure 7.** The 700 hPa vertical  $p$ -velocity (contour interval =  $3 \mu\text{b s}^{-1}$ ) at 1800 UTC 29 November 1991 from (a) NORAPS (Source: Pauley et al. [1996]) and (b) NARR (Source: <http://nomads.ncdc.noaa.gov>; Rutledge et al. [2006]). The accident site is marked by  $\otimes$ .

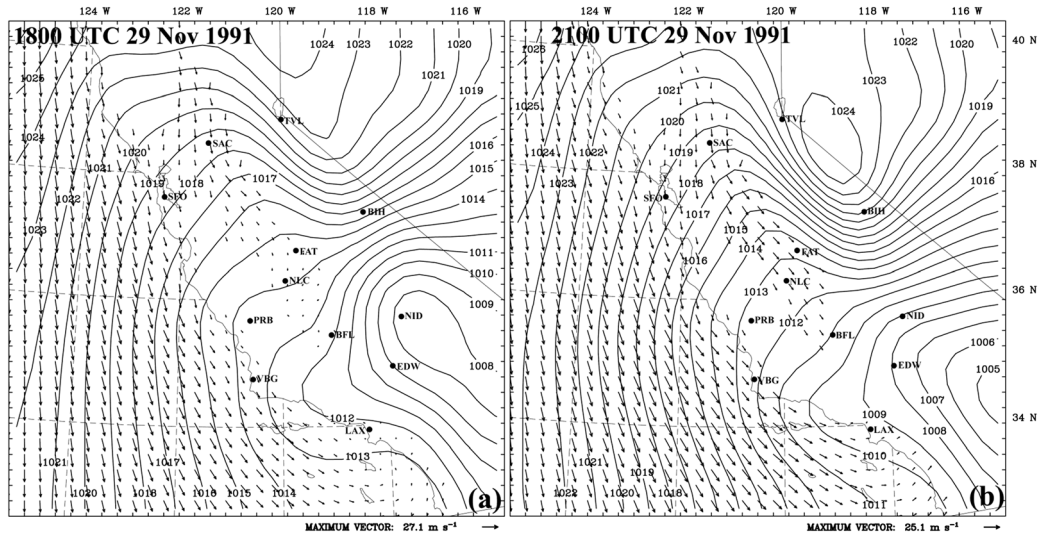


**Figure 8.** Mean sea level pressure ( $P_{MSL}$ ; solid; contour interval=1 hPa) and horizontal winds at 975 hPa from NARR at (a) 1800 UTC and at (b) 2100 UTC 29 November 1991.

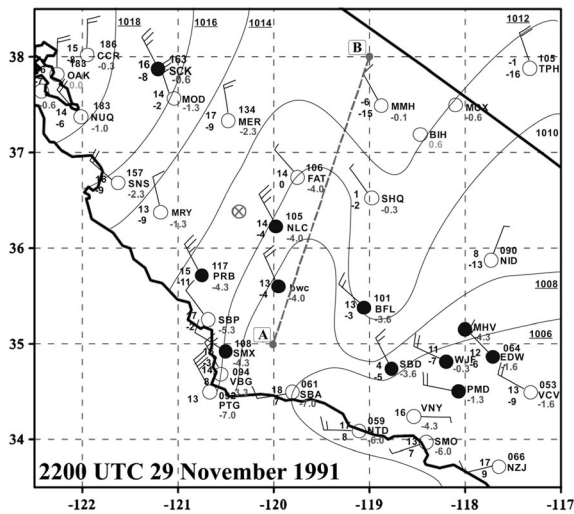


**Figure 9.** Subjectively analyzed  $P_{MSL}$  analysis (modified from Figure 11 of Pauley *et al.* [1996]) at 2200 UTC 29 November 1991. Overlain is the cross-section A-B as shown in Figure 1, and  $\otimes$  marks the accident site.

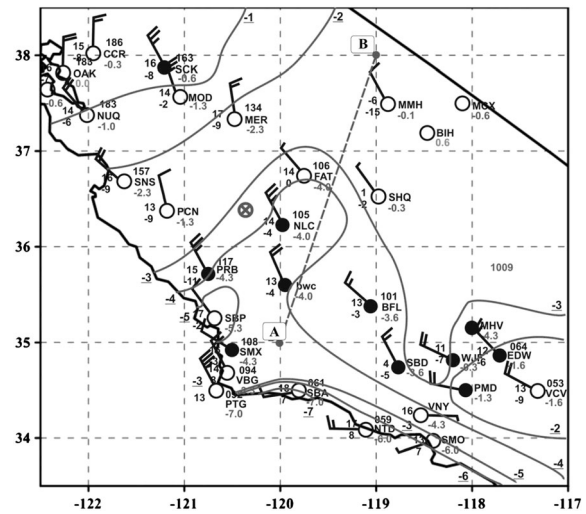


**Figure 10.** Subjectively analyzed  $P_{MSL}$  tendency [ $(\text{hPa } 5\text{h})^{-1}$ ] valid for the period 1700–2200 UTC 29 November 1991. Overlain is the cross-section A-B as shown in Figure 1, and  $\otimes$  marks the accident site.

### 2.3. Geomorphology Near the Accident Site of the Dust Storm

[20] The Landsat-NDVI (Normalized Difference Vegetation Index) [Vogelmann *et al.*, 2001] derived imagery in the vicinity of the dust storm is shown in Figure 11 with superposition of the surface wind direction shown in Figure 9. Figure 11 illustrates the surface conditions in the southern San Joaquin Valley (see Figure 1 for the location) prior to the dust storm on 29 November 1991. The NDVI is illustrated as a continuum with highly vegetated regions (shaded green) and areas of bare ground (shaded dark brown). This continuum permits identification of possible dust sources in the southern San Joaquin Valley. It is likely that the areas shaded in brown (where there was an absence of vegetation) along the western portion of

the southern Valley were sources for dust entrainment. As will be seen later, there was also high-intensity turbulence kinetic energy ( $\text{TKE} > 3.0 \text{ J kg}^{-1}$ ; see also Figure 20) co-located with broad areas of dry, non-vegetated ground along the western portion of the Valley on 29 November 1991. With high winds, adequate near-surface turbulence and limited vegetation to inhibit saltation and entrainment, it is likely that dust entrainment and transport was highly efficient across much of the western portion of the San Joaquin Valley near the I-5 accident site.

### 3. Design of WRF Numerical Experiment

[21] A high-resolution numerical simulation is conducted using the mass core non-hydrostatic Weather Research and

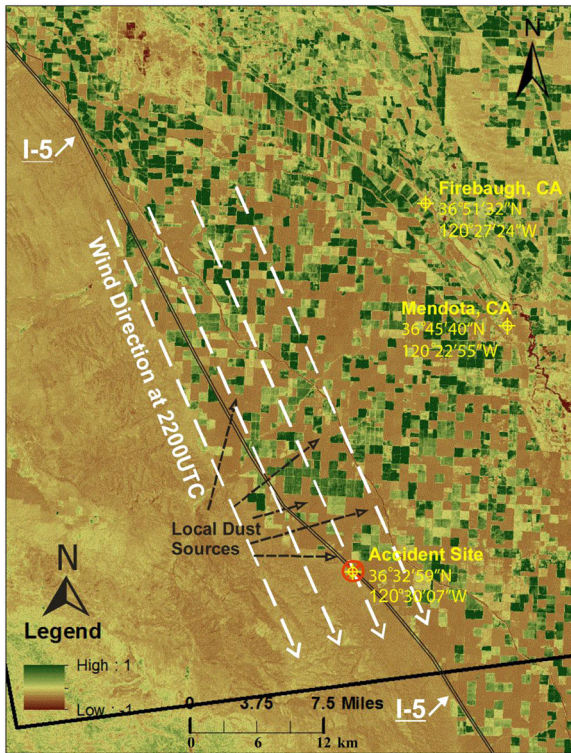


**Figure 11.** NOAA Landsat-NDVI mosaic image of the San Joaquin Valley of California for October 1991. Dashed (white) vectors represent observed wind direction during the dust storm at 2200 UTC 29 November 1991, and dashed (black) vectors point to dust sources. Also shown are the I-5 corridor and the accident site.

Forecasting (WRF) model [Skamarock *et al.*, 2008]. The WRF model is built over a parent domain whose horizontal grid dimensions are  $157 \times 127$  grid points (54 km grid spacing in the horizontal direction) in the west-east and south-north directions, respectively. Three modeling domains are nested into the parent domain consisting of  $247 \times 247$  grid points (18 km grid),  $451 \times 451$  grid points (6 km grid), and the innermost nest has  $721 \times 721$  grid points (2 km grid). The four WRF modeling domains are shown in Figure 12. The interactive strategy between the model domains is one way. The model configuration has 47 levels in the vertical extending up to 15 km AGL; 18 vertical levels were below 1.5 km AGL with the lowest model level set at 10 m AGL.

[22] High-resolution ( $0.08^\circ$ ) datasets of topography, land mask, land use, and 25 vegetation types and 16 soil types archived by the United States Geological Survey (USGS) are used for static fields in the simulations. The model physics includes (i) momentum and heat fluxes at the surface computed using an Eta surface layer scheme [Janjić, 1996, 2001] following Monin-Obukhov similarity theory, (ii) turbulence processes following the Mellor-Yamada-Janjić level 2.5 model [Mellor and Yamada, 1974, 1982; Janjić, 2001], (iii) convective processes following the Betts-Miller-Janjić cumulus scheme [Betts, 1986; Betts and Miller, 1986; Janjić, 1994]—applied only on 54 and 18 km grids—(iv) cloud microphysical processes following explicit bulk representation of microphysics [Thompson *et al.*, 2004, 2006], (v) radiative processes using the Rapid Radiative Transfer Model for long wave radiation [Mlawer *et al.*, 1997] and Dudhia’s short wave scheme [Dudhia, 1989], and (vi) the land-surface processes following the Noah

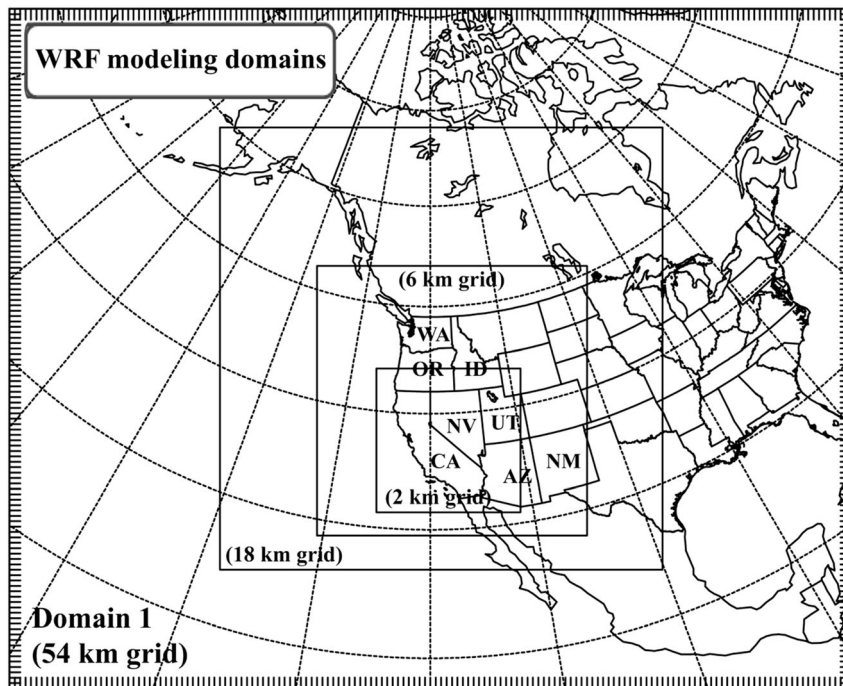


**Figure 12.** WRF modeling domains employed in this study. Also shown are the state identifiers in the western USA [WA= Washington, OR=Oregon, NV=Nevada, CA=California, AZ=Arizona, ID=Idaho, UT=Utah, and NM=New Mexico].

land-surface model (Noah LSM) which provides the surface sensible and latent heat fluxes, and upward longwave and shortwave fluxes to the atmospheric model [Chen and Dudhia, 2001; Ek et al., 2003].

[23] The WRF model was initialized at 0600 UTC 29 November 1991 using 3 hourly NARR datasets. Figure 1 also illustrates three cross-sections A-B (SW-NE orientation focusing on unbalanced ascent), C-D (NW-SE orientation focusing on TKE) and E-F (WSW-ENE orientation focusing on jetlet adjustments) used in the study. The cross-sectional analysis was performed for the *day 2* period and includes vertical motion, isentropes, horizontal winds, and TKE.

#### 4. Mesoscale Results from WRF

[24] We divide our discussion of mesoscale results from WRF into the following subsections: (1) Evolution of jetlet, ageostrophy, and flow in a high Rossby number regime; (2) plan view of lower tropospheric vertical motion and display of vertical motion and thermodynamic structure over the entire troposphere along a judiciously chosen cross section; (3) advance of low-level cold air over the accident site; (4) development of TKE in the planetary boundary layer (PBL); and (5) Lagrangian back trajectories from locations near the accident site.

##### 4.1. Jetlet Evolution

[25] In accordance with the mesoscale wind maximum (jetlet) seen in NARR fields and surface observations during the period 1500–2100 UTC 29 November 1991 (Figures 5–10; section 2), the region between the cross-sections A-B and E-F shown in Figure 1 is the optimal target location for critical mesoscale wind and mass adjustment, in other words, the region encompassing the stations BFL-Bishop (BIH)-NLC-Fresno (FAT)-China Lake (NID). We analyze the cause and consequences of this jetlet closely here using WRF results at a finer spatial and temporal resolution than can be achieved from NARR and surface observations.

[26] Figure 13 shows the wind and vertical motion fields at 1800 UTC 29 November 1991. The focal point for this analysis is the group of mesoscale jetlet features in the vertical layer between isentropic surfaces 295 and 300 K or 700–800 hPa. Isentropic analyses of winds on 297 and 299 K, shown in Figure 13, indicate a narrow (less than 100 km in width) jetlet development in between BFL-BIH-NLC-FAT-NID which is clearly separated from the primary upstream jet streak seen along the California Coast. The jetlet is forced in large part by the terrain-induced west-east mesoscale height gradient in the region between FAT and BIH at 1500 UTC, and subsequently between BFL and NID at 1800 UTC 29 November 1991 (not shown).

[27] A significant height gradient on an isentropic surface portrays a region where isentropes slope substantially, which on a pressure surface is seen as a region of significant temperature gradient. This height gradient is analogous to the temperature gradient over the Sierra Nevada and between the Sierra Nevada and Central Valley of California resulting from the cross-mountain flow on 28 November 1991 (day 1, section 2.1, Figures 3 and 4). The downslope flow produced higher heights in the warm-air side on the western slopes of the Sierra Nevada relative to the cooler air at the same level over the Central Valley of California and also relative to the

cooler air on the eastern windward slope of the Sierra Nevada on day 1. The primary and very large height gradient being oriented west-east over the western Sierra Nevada slope below 700 hPa. The jetlet development on the 299 K isentropic surface occurs over a 3 h period (1500–1800 UTC 29 November 1991) with increasing total wind magnitudes from  $27 \text{ m s}^{-1}$  at 1500 UTC to  $40 \text{ m s}^{-1}$  at 1800 UTC. It represents a fast adjustment because the westerly flow ahead of the large-scale jet streak forces a geostrophic/thermal wind imbalance in the Central Valley region of strong zonal height gradient at the mesoscale. This orientation of this jetlet is in agreement with the orientation of the inverted trough (oriented north-northeast-south-southwest; Figures 9 and 10 along cross-section A-B). The jetlet can also be best seen to the southeast of cross-section A-B along cross-section E-F at 1800 UTC (Figure 13c) as a sloping wind maximum in the 290–300 K layer extending downwards over the western side of the Sierra Nevada crest, i.e., south of BIH.

[28] Ascent in the warm air above the Central Valley of California exists to even above the 310 K isentropic surface (in cross-section E-F in Figure 13c) which clearly signals a thermally direct circulation accompanying this mesoscale feature with rising in the warm leeside air. As will be shown in Figure 16, the ascent maximizes along A-B upstream of the jetlet which is strongest along E-F. This further implies the existence of velocity divergence west of the Sierra Nevada along A-B accompanying this feature thus inducing pressure falls close to the location of the aforementioned inverted trough between FAT and the California coast (Figures 9 and 10) along cross-section A-B centered in time at 1800 UTC 29 November 1991. Note that the ascent at 1800 UTC was virtually absent in this location 3 h earlier along the cross-section A-B which clearly signals the explosive development (highly accelerative) and southward propagation of this mesoscale feature and its divergence ahead of the larger-scale jet streak and behind the mesoscale jetlet.

##### 4.2. Ageostrophy Evolution and Distribution of the Lagrangian Rossby Number

[29] The Lagrangian Rossby number,  $Ro^L$ , has been used to advantage in earlier synoptic-mesoscale studies that have aimed to identify regions of mesoscale motions [e.g., Van Tuyl and Young, 1982; Zack and Kaplan, 1987; Koch and Dorian, 1988; Zhang et al., 2000; Kaplan et al., 2011]. In essence, this number is a ratio of wind magnitudes, the ratio of ageostrophic wind ( $\vec{V}_{ag}$ ) magnitude to the magnitude of the entire horizontal wind ( $\vec{V}_H$ ). The mathematical form of this ratio is

$$Ro^L = \frac{\left| \frac{\partial \vec{V}_H}{\partial t} + (\vec{V}_H \cdot \nabla) \vec{V}_H \right|}{f \left| \vec{V}_H \right|} \quad (2)$$

where  $\nabla$  is the horizontal gradient vector.  $Ro^L \geq 0.5$  generally represents a strongly accelerative mesoscale flow and is labeled a “high Rossby number regime”, whereas  $Ro^L \sim 0.1$  is weakly accelerative and characterizes a Q-G regime (see review in Zhang et al. [2000]). In our domain of interest, notably over central and southern California,  $Ro^L$  has been calculated at low-, mid-, and high-levels in the troposphere

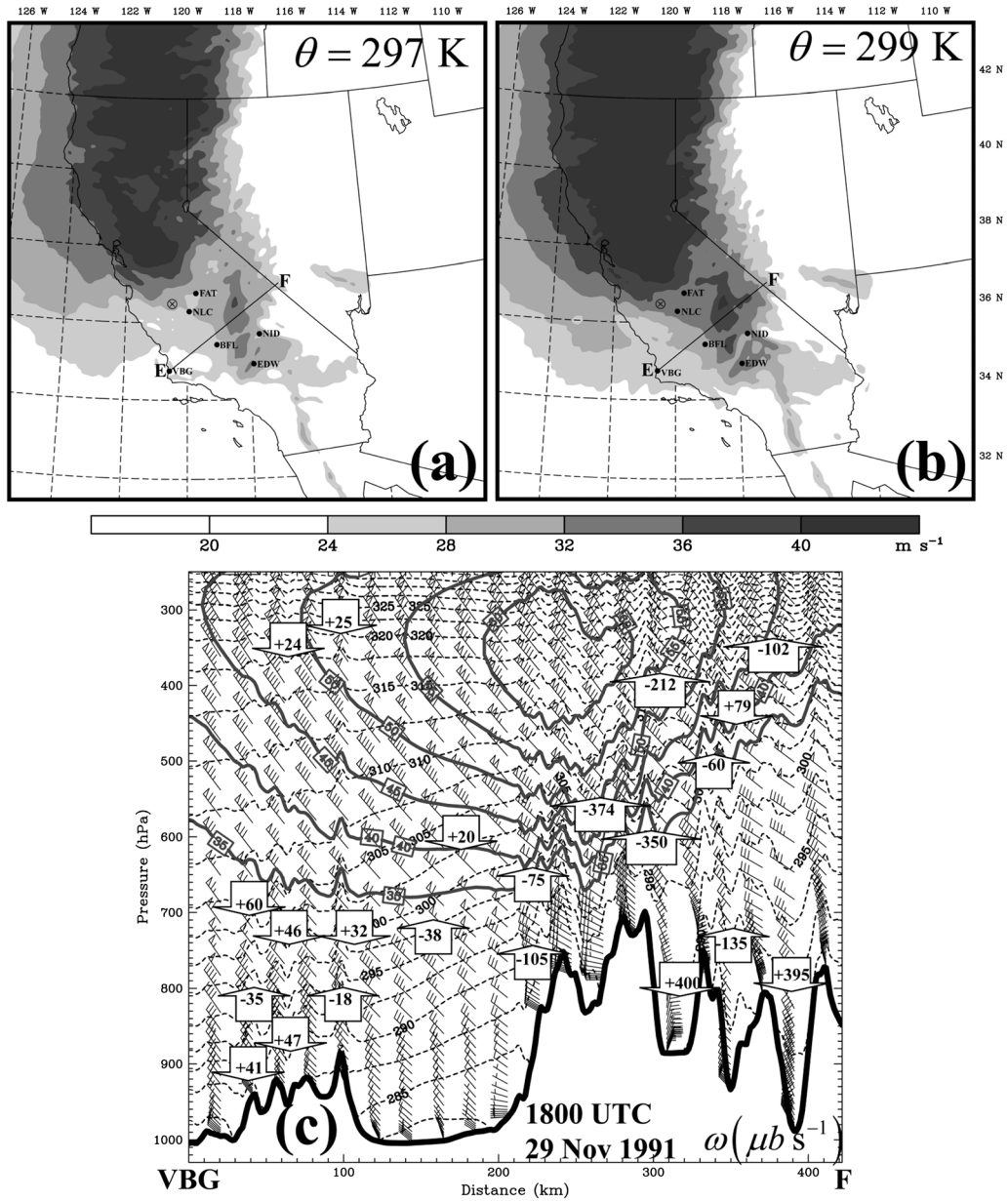


**Figure 13.** Horizontal wind speeds [isotachs (shaded)] valid at 1800 UTC 29 November 1991 on the isentropic surfaces (a) 297 K and (b) 299 K. (c) Potential temperature ( $\theta$ ; dashed; contour interval = 2 K), vertical p-velocity (magnitudes given in  $\mu\text{b s}^{-1}$ ), and horizontal winds [full barb = 5  $\text{m s}^{-1}$ ; isotach contour (solid) interval = 5  $\text{m s}^{-1}$ ] along the cross-section E-F from WRF (2 km grid).  $\otimes$  marks the accident site. The closest location to BFL along E-F is at 160 km.

over the 12 h period preceding the onset of the dust storm. The high  $Ro^L$  regimes were only significant at lower tropospheric levels (below 675 hPa) and diminished in magnitude aloft.

[30] Figures 14 and 15 show the evolution of the 775 hPa ageostrophic wind component and Lagrangian Rossby numbers during the 1500–1800 UTC period on 29 November 1991 focusing on the region surrounded by the stations BFL-NLC-FAT-BIH-NID. A narrow region of eastward-directed ageostrophic flow develops within the broader northward-directed ageostrophic flow region northwest of BFL and then builds southeastwards as the predominantly westerly ageostrophic component intensifies nearly  $13 \text{ m s}^{-1}$

in 3 h just west of the Sierra Nevada from BIH southward to near NID as explained above.

[31] The  $Ro^L$  values, which are indicative of a Lagrangian acceleration of this extraordinary magnitude, increase in isolated locations by 1800 UTC 29 November 1991 to much greater than 1 in magnitude in the region bounded by BFL-NLC-FAT-BIH-NID. This indicates that the jetlet is developing within the larger-scale geostrophic jet streak's exit region and is highly accelerative accompanying a thermally direct ageostrophic circulation—not decelerative indirect circulation. The velocity divergence northwest of the jetlet and southeast of the I-5 accident location accompanying this circulation organizes the ascent, pressure falls,

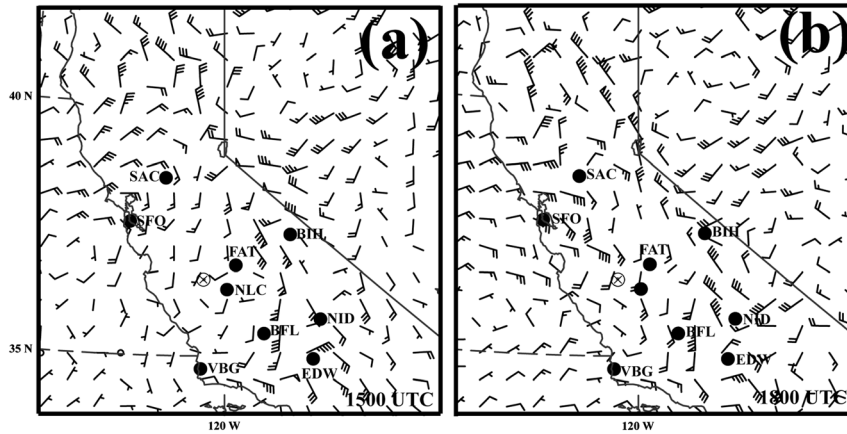


**Figure 14.** The 775 hPa ageostrophic winds (full barb =  $5 \text{ m s}^{-1}$ ) from WRF (6 km grid) at (a) 1500 UTC and (b) 1800 UTC 29 November 1991.  $\otimes$  marks the I-5 accident site.

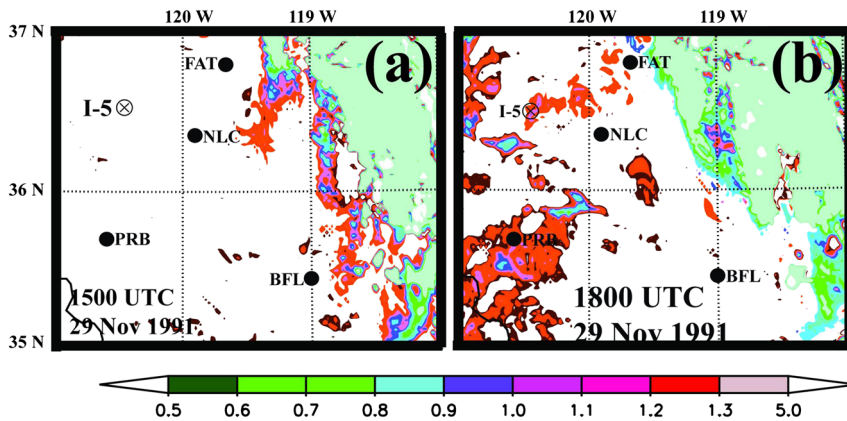


**Figure 15.** The 775 hPa Lagrangian Rossby Numbers (equation (2)) diagnosed from WRF (2 km grid) at (a) 1500 UTC and (b) 1800 UTC 29 November 1991.  $\otimes$  marks the I-5 accident site.

and adiabatic cooling along cross-section A-B during 1700–1800 UTC 29 November 1991 (Figure 16). The WRF simulation represents yet additional evidence of the highly accelerative and thermally direct nature of this feature resulting from the interaction between the southward-propagating quasi-geostrophic jet streak’s exit region and the previous day’s mesoscale baroclinic zones along the west side of the Sierra Nevada Mountains.

#### 4.3. Vertical Motion

[32] Figure 16 shows two different perspectives of 775 hPa vertical motion ( $\omega$ ) during 1700–1800 UTC 29 November 1991. The panels show the southward advancement of 775 hPa lifting that is just upstream from the ageostrophy and high  $Ro^L$  regime shown in Figures 14 and 15, i.e., primarily in the region surrounding the stations BIH-FAT-NLC-BFL-EDW-NID. Notable features in the vertical motion, shown in Figure 16, are the following: (i) lifting that occurs behind the synoptic-scale low-pressure center in extreme southeastern California—in opposition to the anticipated descent from Q-G theory—and (ii) the presence of an extremely small scale ascent-descent-ascent structure at 1800 UTC 29 November 1991 southeast of the accident site

between BIH, FAT, NLC, BFL, EDW, and NID. The distance between the ascent centers is the order of 30–60 km.

[33] Both NARR and WRF generate ascent south of TVL at 1500 UTC, and this feature tracks southward into the area bounded by the stations PRB-FAT-BFL by 1800 UTC. The bifurcation noted in (ii) adds detail to the general area of 700 hPa ascent seen in the NARR vertical motion fields in between PRB-FAT-BFL (Figure 7). These small-scale features are consistent with observed mesoscale  $P_{\text{MSL}}$  fall zones seen in NARR and the surface observations described earlier in section 2. They also closely align with the location of maximum cross-stream ageostrophy and the intensifying  $Ro^L$  distribution shown in Figures 14 and 15 (especially near NLC). It should be mentioned that there is no lifting at the upper tropospheric levels between 1700 and 1800 UTC 29 November 1991 (not shown).

[34] The vertical motion, isentropes, and horizontal winds along the cross-section A-B (Figure 1) that cuts across the San Joaquin Valley and borders the accident site at 1700 and 1800 UTC 29 November 1991 are shown in Figures 16c and 16d. Note that this cross-section A-B is closely aligned with the inverted trough shown in Figures 9 and 10. At 500 hPa and higher levels, the vertical motion is weakly

downward in Figures 16c and 16d (above the region of thermally direct ascent below 500 hPa in conjunction with the inverted trough). That is, there is evidence of a larger-

scale weak indirect circulation—a Q-G circulation about the jet in support of Danielsen's paradigm but in the company of a larger magnitude mesoscale ascent at lower

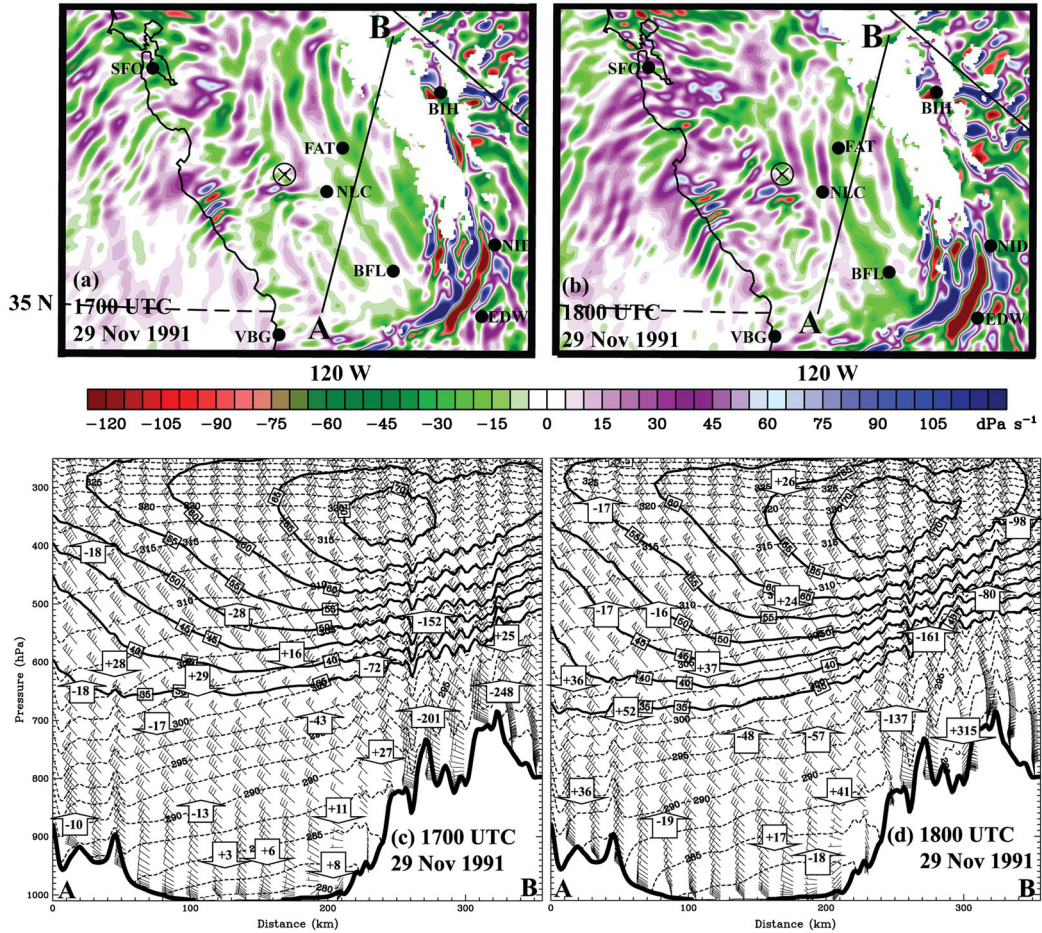


**Figure 16.** Plan view of 775 hPa vertical p-velocity ( $\mu\text{b s}^{-1}$ ) from WRF (2 km grid) valid at (a) 1700 UTC and (b) 1800 UTC 29 November 1991. High-elevated regions (surface pressure < 775 hPa) are masked in the figure. Also shown in this figure is the cross-section A-B, along which potential temperature (dashed; contour interval = 2 K), vertical p-velocity (arrows;  $\mu\text{b s}^{-1}$ ), and horizontal winds (isotachs—solid; contour interval = 5  $\text{m s}^{-1}$ , and full barb = 5  $\text{m s}^{-1}$ ) are shown at these times (c and d).

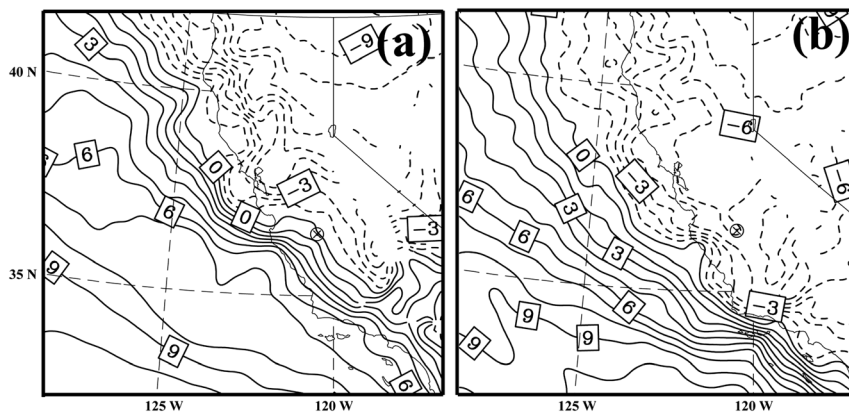


**Figure 17.** The 800 hPa air temperature (contour interval = 1°C; positive—solid contours; negative—dashed) from WRF (6 km grid) at (a) 1800 UTC 29 November 1991 and (b) 0000 UTC 30 November 1991. The accident site is marked by  $\otimes$ .

levels. The upper level descent above 600 hPa over coastal California is skewed well to the west of the ascent below 600 hPa over the Central Valley.

[35] The region of strongest lifting over the west and east slope of the Sierra is not the result of orographic lift—the flow at mountaintop levels and lower is parallel to the crest. Rather, this mesoscale lifting is associated with the high  $Ro^L$  regime and its accompanying divergence that builds in time from SAC to NID. Cross-section A-B extends through this region of ascent located just north of BIH. Notice that the vertical motion over the accident site (the closest location to the accident site is NLC which is approximately located at 150 km along A-B) is about  $-40 \mu\text{b s}^{-1}$ . During the 1600–1800 UTC period, the ascent plume above the west slopes of the Sierra Nevada north of BIH builds downward and southwestward toward the region just south of the accident location as a sloping feature. This reflects the mass removal from the column associated with the accelerating mesoscale jetlet west of the Sierra Nevada described earlier.

**4.4. Cold Air Advance**

[36] Figure 17 shows the evolution of 800 hPa air temperature during 1800 UTC 29 November 1991–0000 UTC 30 November 1991 period. Note that the advance of cold air in the lower troposphere is associated with the mesoscale ascent described in the previous subsection. Figure 17 clearly shows 800 hPa cooling that propagates southward and westward in the high  $Ro^L$  regime. The cooling is a response to the unbalanced ascent in Figure 16 and the subsequent west-southwesterly advection of this newly generated mesoscale tongue of cold air. Also notable is the region of ageostrophic/isalobaric winds that converges on the accident site between 1700 UTC and 2200 UTC (Figure 18). This convergence into the simulated  $P_{\text{MSL}}$  fall zone is consistent

with the observed inverted trough and accelerating northwesterly flow shown along A-B in Figures 9 and 10.

[37] Figures 19a and 19c show the simulated sounding at the accident site valid at 1500 UTC and at 2100 UTC 29 November 1991 as well as comparisons with observed surface winds at NLC. During the early part of this period, the simulated soundings show dramatic cooling below

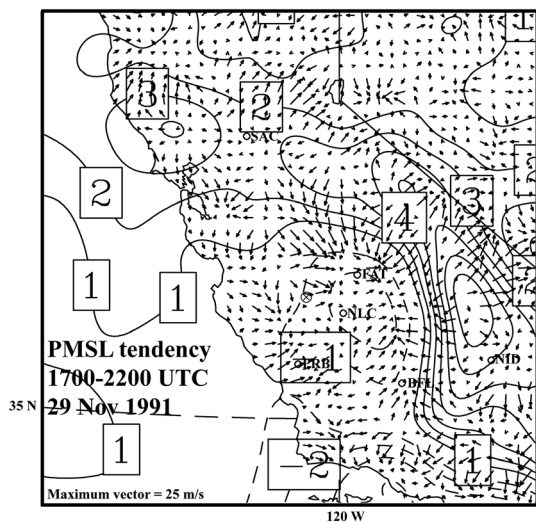


**Figure 18.** The 5 h  $P_{\text{MSL}}$  tendency (contour interval = 1 hPa) and isalobaric winds (see equation (1)) diagnosed from WRF (6 km grid) valid for the period 1700–2200 UTC 29 November 1991. The accident site is marked by  $\otimes$ . Maximum vector =  $25 \text{ m s}^{-1}$ .

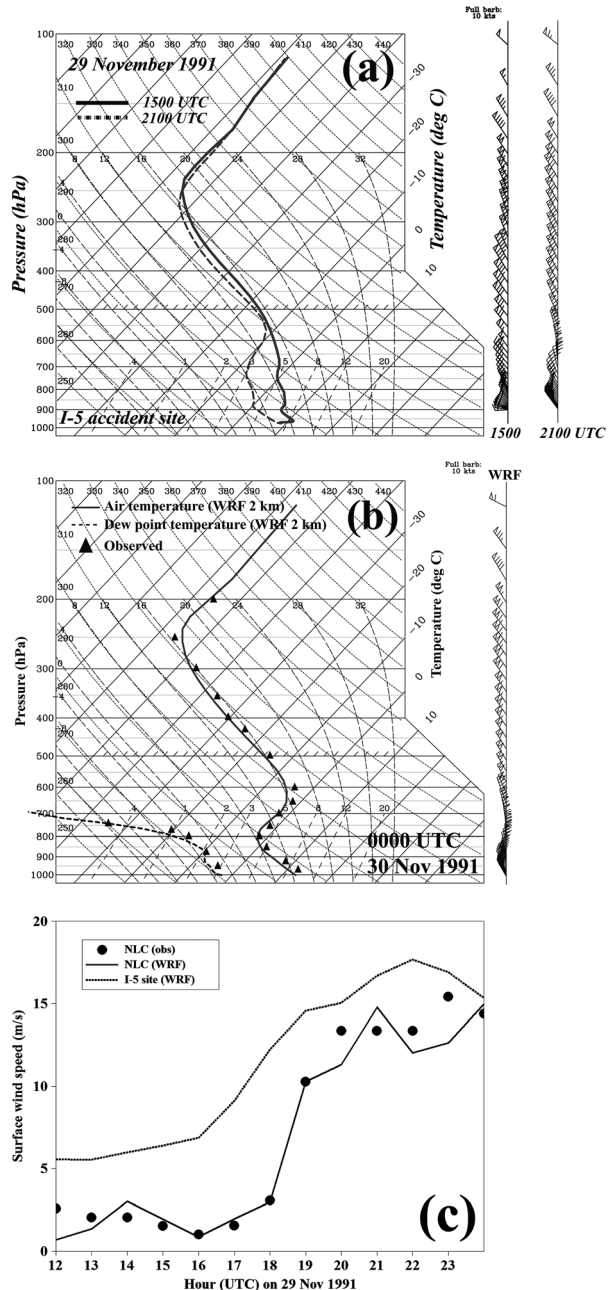


**Figure 19.** WRF (2 km grid) simulated (a) temperature ( $^{\circ}\text{C}$ ) and horizontal winds (full barb =  $5 \text{ m s}^{-1}$ ) at the accident location (Figure 1) at 1500 UTC and 2100 UTC 29 November 1991, (b) observed and simulated sounding at VBG at 0000 UTC 30 November 1991, and (c) observed and simulated time series of surface wind speed (solid line;  $\text{m s}^{-1}$ ) at Lemoore (NLC). Also shown is the model simulated wind speeds (dashed) at the I-5 accident site.

600 hPa at the accident location— $7^{\circ}\text{C}$  cooling at 800 hPa over the 6 h period (Figure 19a). The cooling only occurs in the low troposphere—600 hPa and lower—and is closely aligned in time with inverted trough formation between 1700 and 2200 UTC and accelerating surface wind flow which is also evident at NLC in both WRF and the observations during the 1800–2100 UTC period (Figure 19c).

[38] The observed cooling rates in the lower troposphere at VBG (Figure 19b) and EDW are consistent with the simulated cooling rates (about  $1^{\circ}\text{C h}^{-1}$ ). Additionally, upper air observations from aircraft that flew over SAC during 1300–1900 UTC 29 November 1991 support this cooling as well (cf. Figure 13 of Pauley *et al.* [1996]).

#### 4.5. Turbulence Kinetic Energy (TKE)

[39] Figure 20 shows the development of TKE in the planetary boundary layer along the cross-section C-D (see Figure 1 for the location) in the San Joaquin Valley of California at 1800 UTC and at 2100 UTC 29 November 1991, respectively. A well-mixed layer is evident from the near constancy of the potential temperature (285 K) between the surface and 900 hPa. The largest magnitude values of TKE ( $>3\text{ J kg}^{-1}$ ) occur at the accident site and 100 km to the northwest of the site. This dry adiabatic layer is consistent with that observed at SAC at 1900 UTC (cf. Figure 13 of Pauley *et al.* [1996]; the left end of the cross-section C-D is located at SAC—see Figure 1) and propagates toward the accident location and NLC by 2100 UTC 29 November 1991 (Figure 19c). The cold pool at 800 hPa which supports the development of the well-mixed layer moves southwestwards in concert with the accelerating north-northwesterly ageostrophic/isallobaric flow as can be seen in Figure 17. The TKE develops near the surface within the adiabatic layer coinciding with the observed and simulated strongest surface winds in the vicinity of the I-5 accident site (Figures 19a, 19c, and 20).

#### 4.6. Lagrangian Back Trajectories

[40] Figure 21 shows the Lagrangian back trajectories initiated from locations near the accident site ( $36.5^{\circ}\text{N}$ ,  $120.5^{\circ}\text{W}$ , FAT, and NLC) and time (2200 UTC 29 November 1991). Trajectory 1 is initiated at and moves backwards in time from the 900 hPa level above the accident site—near the top or within the mixed layer. Similarly, trajectories 2 and 3 are initiated at NLC and FAT, respectively. All trajectories extend backward in time to 0600 UTC 29 November 1991 (a track of 16 h duration). Although the initiation points of trajectories 1, 2, and 3 lie within a circle of radius of about 50 km, significant variance in the pathways backwards in space and time is evident from Figure 21. Figure 22 shows the Lagrangian parcel diagnostics for the trajectory 1 (not shown for trajectories 1 and 2) and indicates that extreme variance in the accelerations and warming/cooling along the pathway was evident.

[41] Trajectory 1 exhibited a short period of extreme ascent 3 h prior to its arrival over the accident site, whereas the other two trajectories exhibited short-lived weak ascent and short-lived strong descent, respectively, prior to arriving at their respective locations. At the time of trajectory termination and shortly before, i.e., at and shortly after 0600 UTC, trajectory 1 shows little forward motion because it resides under the high-pressure region in between the two Q-G jet streaks described in section 2. At 0600 UTC, the parcels for trajectories 2 and 3 reside in the 700–800 hPa layer and are approximately 1000 km from their initiation points. That is, the pressure differential between beginning and ending points on these trajectories is about 200 hPa. The parcel associated with trajectory 1 slowly descended from 850 hPa prior to its abrupt ascent and cooling during the last several hours.

[42] Parcel accelerations of  $15\text{--}20\text{ m s}^{-1}$  (Figure 22) occurred over the last several hours for trajectory 1 and nearly as much for trajectory 2 in the presence of slight deceleration and 3 h descent/warming during this period for trajectory 3

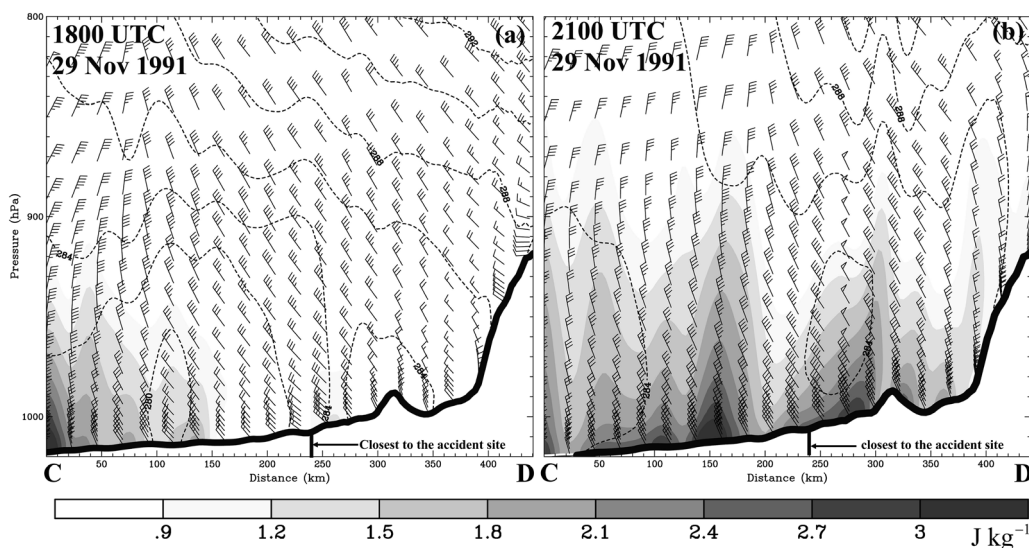


**Figure 20.** Potential temperature (dashed; contour interval = 2 K), horizontal winds (full barb =  $5\text{ m s}^{-1}$ ), and turbulence kinetic energy (TKE; shaded;  $\text{J kg}^{-1}$ ) along the cross-section C-D from WRF (6 km grid) valid at (a) 1800 UTC and at (b) 2100 UTC 29 November 1991. Also marked is the closest location to the accident site along the cross section at 240 km.

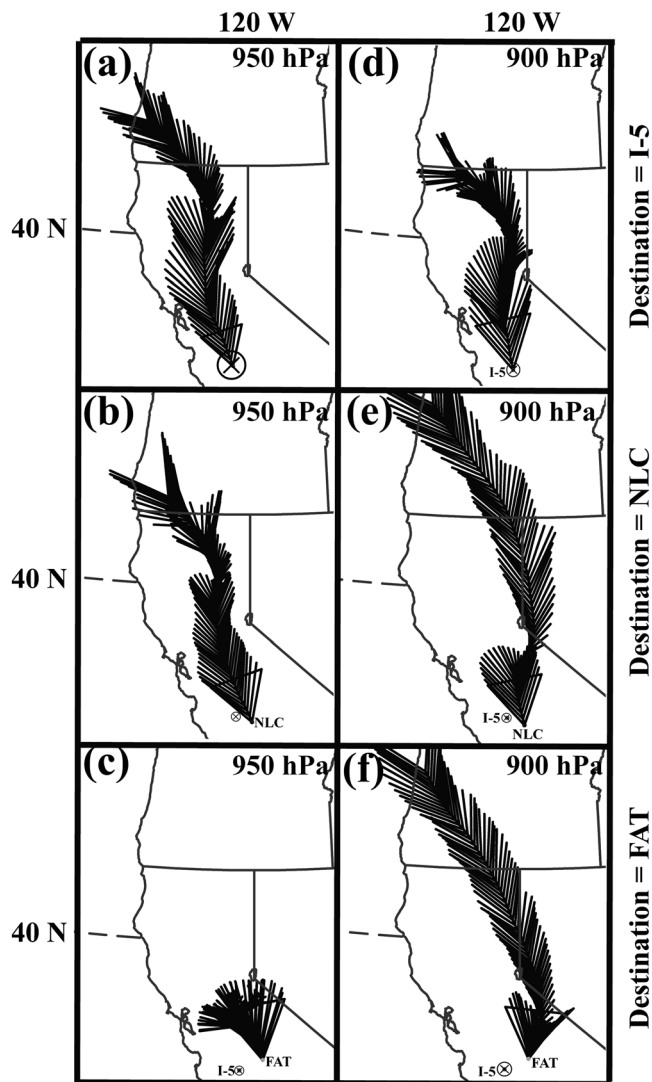


**Figure 21.** WRF (18 km grid) diagnosed Lagrangian back trajectories ending at (a–c) 950 hPa and (d–f) at 900 hPa above (1) the accident location (Figures 21a and 21d), (2) Lemoore (Figures 21b and 21e), and (3) Fresno (Figures 21c and 21f). Back trajectories are traced back from 2200 UTC to 0600 UTC 29 November 1991. Arrows are shown at every 10 min interval. Wider (narrower) arrows indicate regions of parcel ascent (descent). The accident site is marked by  $\otimes$ .

(not shown). This 3 h terminal cooling above the accident site in association with heating at the surface leads to deepening and further destabilization of the near-surface layer. The cooling and accelerations reflect the isallobaric/ageostrophic flow just upstream from the accident location and NLC. Blowing dust occurs, i.e., at initiation points of trajectories 1 and 2. Blowing dust is not present at FAT where stabilization is occurring.

[43] Consistent with destabilization accompanying parcel ascent for trajectories 1 (Figure 22) and 2, there is a dramatic increase in parcel accelerations, TKE,  $P_{MSL}$  change, and PBL depth between 1900 and 1600 UTC 29 November 1991. These changes were important to the creation of the

well-mixed PBL inferred from Figure 20. The acceleration, ascent, and cooling of the air at the accident site accompanying trajectory 1 are certainly in opposition to the view of trajectory characteristics in Danielsen’s paradigm—namely, elongated Q-G trajectories that descend from the lower stratosphere to the earth’s surface while exhibiting deceleration and warming. A cursory analysis of ozone data from the Total Ozone Mapping Spectrometer (TOMS) instrument gave no evidence of infusion of stratospheric air into the troposphere over California. Only a modest increase in ozone was found in southern Nevada and points eastward over the 24 h period preceding the dust storm.

## 5. Discussion and Conclusions

[44] Pauley *et al.* [1996] originally investigated the Interstate 5 (I-5) dust storm with the aid of a rather coarse by today’s standards (60 km grid resolution) U. S. Navy operational data assimilation scheme (optimal analysis) and an equally coarse background forecast. It was the subjective surface pressure analysis and thermodynamic profiles from an instrumented aircraft that delivered some hint of the operative smaller-scale processes germane to storm generation. Through use of the recently available NARR reanalysis dataset and very high resolution numerical simulations from the state-of-the-art Weather Research and Forecasting (WRF) model, we have now been able to couple mesoscale processes that offer a coherent view of dust storm generation—an alternate and in some sense a complementary view of storm generation compared to Danielsen’s [1974] classic view. Whereas the processes identified by Danielsen are associated with the dynamics of Q-G theory, and in particular with the mechanics of larger-scale and slower cyclogenetic systems, the processes identified in this study are more representative of the smaller or intermediate scales of motion—still baroclinic but secondary to the larger-scale cyclogenetic processes and certainly not in thermal wind balance.

[45] As opposed to the importance of long descending/ decelerating flows along isentropic trajectories associated with tropopause folds, i.e., the central features of the Danielsen paradigm, this study places emphasis on mesoscale adjustments linked to larger-scale imbalance. These adjustments lead to destabilization of the boundary layer, production of ageostrophic/isallobaric winds and associated turbulence kinetic energy that is necessary to ablate the dust. Further, this study links geostrophic imbalance to a sequence of larger-scale disturbances—a setup day where a mass/temperature field and associated extreme geostrophic wind lays in wait for the intrusion of momentum from an upstream jet streak. The imbalance between the intruding momentum and the extreme geostrophic wind requires fast adjustment on the order of 6–12 h, a fraction of the pendulum day time scale for Q-G dynamics.

[46] In summary, the key elements of the mesoscale adjustment are direct transverse circulation about the jet (lifting on the warm-air side of the jet), cooling due to the ascent and subsequent cold air advection, and the associated re-adjustment of the mass field that leads to low-level ageostrophic/isallobaric wind. Back trajectories from locations near the accident site give evidence of mesoscale variance in pathways and hydro-thermodynamic characteristics of parcels where the ascent/cooling and destabilization

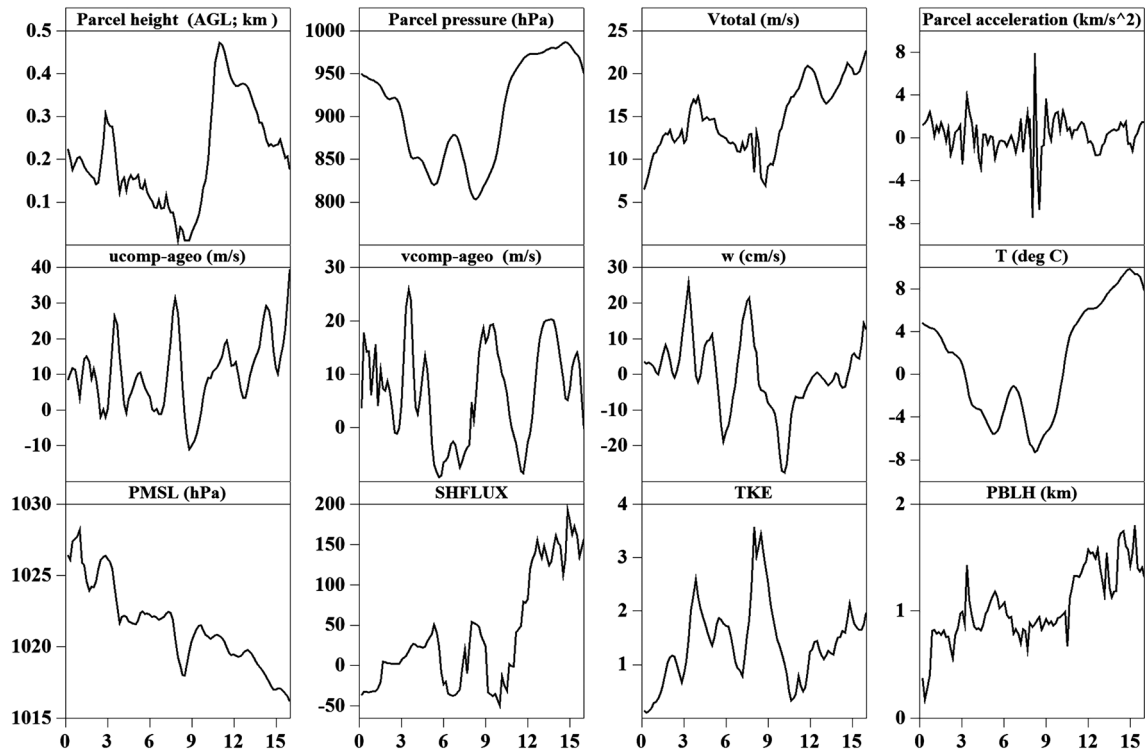


**Figure 22.** Lagrangian parcel diagnostics for trajectory 1 (parcel terminates at 950 hPa above the accident site at 2200 UTC 29 November 1991—Figure 21a). Time series of parcel’s height (agl; km), pressure (hPa), horizontal wind speed ( $\text{m s}^{-1}$ ), parcel acceleration ( $\times 10^3 \text{ m s}^{-2}$ ), components of ageostrophic wind ( $\text{m s}^{-1}$ ), vertical velocity ( $\text{cm s}^{-1}$ ), air temperature ( $^{\circ}\text{C}$ ), mean sea level pressure (hPa), sensible heat flux ( $\text{W m}^{-2}$ ), turbulence kinetic energy ( $\text{J kg}^{-1}$ ), and mixed layer depth (km).  $X$  axis represents the time (0 = 0600 UTC 29 November 1991).

of the boundary layer are critical for pinpointing the likely location and timing of dust ablation.

[47] In the absence of soil structure and soil moisture considerations, which are beyond the scope of this manuscript, the dynamical control on event initiation is strongly coupled to surface accelerations and planetary boundary layer (PBL) destabilization due to ascent and cold air advection. This is most likely to occur where there is a rapidly developing surface pressure gradient force in proximity to strong cold air advection within the PBL. This region is the most favored for a TKE “front” to develop within. This would be downstream from a thermally direct ageostrophic circulation in the lower middle troposphere. The most important mechanism responsible would be the thermally direct ageostrophic circulation well below 500 hPa within a region of background substantial lower tropospheric kinetic energy such as a strong low-level jet.

[48] When the study of the I-5 dust storm by Pauley *et al.* [1996] is meshed with this later study, it becomes clear that the limitations of the numerical models of earlier years are likely to miss important smaller-scale processes, or more importantly, they are likely to miss the crucial-scale interaction processes that abound in our complex atmospheric system. That is not to say that the larger-scale aspects of dust storm generation as pioneered by Danielsen [1968, 1974] and others are less important than the unresolved scales in the earlier analyses and models, rather that the smaller-scale processes can now be explored with the benefit of datasets such as NARR and numerical models such as WRF.

[49] The existence of the mass and momentum adjustments which are diagnosed in the manuscript is relatively ubiquitous whenever very strong and spatially expansive large-scale jets interact with complex terrain features. The mechanism is strongly coupled to the scale and orientation of the terrain and the jet streak. In the present study, strong cross-mountain flow with the precursor day’s jet streak established a meso-scale orographic front/baroclinic zone on the western side of the Sierra Nevada that was subsequently perturbed by the second day’s jet streak’s exit region which leads to strong velocity divergence tendencies.

[50] We have examined other case studies such as the one described in the present study that occur regularly on the lee (eastern) side of the Rocky Mountains in New Mexico and Colorado, the Sierra Madre Mountains in northern Mexico, and the Snake River/Bitterroot Mountains in southern Idaho/Montana. In these case studies, the downstream part of the jet’s exit region established a baroclinic zone due to cross-mountain flow only to be perturbed in a likely manner to the I-5 dust storm event of the present study by the upstream part of the jet’s exit region. In these other case studies, the jet and mountain orientations were different, but the physical processes were rather similar, only more closely aligned in space and time.

[51] We are intuitively confident that these adjustments, while not exclusively limited to mountains, are frequently occurring near mountains whenever strong jets pass over mountains. Furthermore, we see no reason why they may not be occurring away from mountains as well, as when a

residual baroclinic zone accompanying a previously generated front or a mesoscale convective system is intercepted by another upstream jet streak.

[52] **Acknowledgments.** The authors thank Robert Rabin of NOAA/NSSL for providing the satellite imagery that aided in the analysis of the dust storm.

## References

- Barker, E. H. (1992), Design of the Navy's multivariate optimum interpolation analysis system, *Wea. Forecasting*, *7*, 220–231.
- Betts, A. K. (1986), A new convective adjustment scheme. Part I: Observational and theoretical basis, *Q. J. R. Meteorol. Soc.*, *111*, 1306–1335.
- Betts, A. K., and M. J. Miller (1986), A new convective adjustment scheme. Part II: Single column tests using GATE WAVE, BOMEX, ATEX and Arctic air-mass data sets, *Q. J. R. Meteorol. Soc.*, *112*, 693–709.
- Bluestein, H. B. (1992), *Synoptic-Dynamic Meteorology in Midlatitudes. I: Principles of Kinematics and Dynamics*, 448 pp., Oxford University Press, USA.
- Chen, F., and J. Dudhia (2001), Coupling an advanced land surface-hydrology model with the Penn State-NCAR MM5 modeling system. Part I: Model implementation and sensitivity, *Mon. Weather Rev.*, *129*, 569–585.
- Covitz, C. D., M. J. Hannigan, J. W. Van Loben Sels, and R. Andrews (1992), Dust-related Collisions, Interstate 5, Panoche Junction Overcrossing/Kamm Avenue, 29 November 1991, State of California, Business, Transportation, and Housing Agency, Sacramento, CA.
- Danielsen, E. F. (1968), Stratospheric-tropospheric exchange of radioactivity, ozone, and potential vorticity, *J. Atmos. Sci.*, *25*, 502–518.
- Danielsen, E. F. (1974), The relationship between severe weather, major dust storms and rapid large-scale cyclogenesis, Sub-synoptic extra-tropical weather systems: observation, analysis, modeling and prediction, *Notes from a Colloquium, Seminars and Workshop*, National Center for Atmospheric Research, pp. 215–241.
- Dudhia, J. (1989), Numerical study of convection observed during the Winter Monsoon Experiment using a mesoscale two-dimensional model, *J. Atmos. Sci.*, *46*, 3363–3391.
- Ek, M. B., K. E. Mitchell, Y. Lin, E. Rogers, P. Grummann, V. Koren, G. Gayno, and J. D. Tarpley (2003), Implementation of Noah land surface model advances in the National Centers for Environmental Prediction operational mesoscale Eta model, *J. Geophys. Res.*, *108*(D22), 8851, doi:10.1029/2002JD003296.
- Hodur, R. M. (1987), Evaluation of a regional model with an update cycle, *Mon. Weather Rev.*, *115*, 2707–2718.
- Janjić, Z. I. (1994), The step-mountain Eta coordinate model: Further developments of the convection, viscous sublayer, and turbulence closure schemes, *Mon. Weather Rev.*, *122*, 927–945.
- Janjić, Z. I. (1996), The surface layer in the NCEP Eta model, Preprints, *11th Conf. on Numerical Weather Prediction*, Norfolk, VA, Amer. Meteor. Soc., pp. 354–355.
- Janjić, Z. I. (2001), Nonsingular implementation of the Mellor-Yamada level 2.5 scheme in the NCEP Meso model, NCEP Office Note, No. 437, 61 pp.
- Kaplan, M. L., R. K. Vellore, J. M. Lewis, and M. Young (2011), The role of unbalanced mesoscale circulations in dust storms, *J. Geophys. Res.*, *116*, doi:10.1029/2011JD016218.
- Koch, S. E., and P. B. Dorian (1988), A mesoscale gravity wave event observed during CCOPE. Part III: Wave environment and probable source mechanisms, *Mon. Weather Rev.*, *116*, 2570–2592.
- Lewis, J. M., M. L. Kaplan, R. Vellore, R. M. Rabin, J. Hallett, and S. Cohn (2011), Dust storm over the Black Rock Desert: Large-scale dynamic signatures, *J. Geophys. Res.*, *116*, doi:10.1029/2010JD014784.
- Liou, C.-S., R. M. Hodur, and R. H. Langland (1994), Navy Operational Atmospheric Prediction System (NORAPS): A triple nested mesoscale model, Preprints, *10th Conf. on Numerical Weather Prediction*, Portland, OR, Amer. Meteor. Soc., pp. 423–425.
- Martin, J. E. (2006), *Mid-latitude Atmospheric Dynamics: A First Course*, 363 pp., John Wiley & Sons, England.
- Martin, J. E. (2008), A southern Plains wintertime dust storm associated with a robust upper-level front [Available at: [http://marrella.meteor.wisc.edu/Martin\\_2008.pdf](http://marrella.meteor.wisc.edu/Martin_2008.pdf)].
- Mellor, G. L., and T. Yamada (1974), A hierarchy of turbulence closure models for planetary boundary layers, *J. Atmos. Sci.*, *31*, 1791–1806.
- Mellor, G. L., and T. Yamada (1982), Development of a turbulence closure model for geophysical fluid problems, *Rev. Geophys. Space Phys.*, *20*, 851–875.
- Mesinger F., et al. (2006), North American Regional Reanalysis, *Bull. Am. Meteorol. Soc.*, *87*, 343–360, doi:10.1175/BAMS-87-3-343.
- Mlawer, E. J., S. J. Taubman, P. D. Brown, M. J. Iacono, and S. A. Clough (1997), Radiative transfer for inhomogeneous atmosphere: RRTM, a validated correlated-k model for the longwave, *J. Geophys. Res.*, *102*(D14), 16663–16682.
- Orlanski, I. (1975), A rational subdivision of scales for atmospheric processes, *Bull. Am. Meteorol. Soc.*, *56*, 527–530.
- Pauley, P. M., N. L. Baker, and E. H. Barker (1996), An observational study of the “Interstate 5” dust storm case study, *Bull. Am. Meteorol. Soc.*, *77*, 693–720.
- Rochette, S. M., and P. S. Market (2006), A primer on the ageostrophic wind, *Natl. Wea. Dig.*, *30*, 17–28.
- Rutledge, G. K., J. Alpert, and W. Ebuisaki (2006), NOMADS: A Climate and Weather Model Archive at the National Oceanic and Atmospheric Administration, *Bull. Am. Meteorol. Soc.*, *87*, 327–341, doi:10.1175/BAMS-87-3-327.
- Schultz, J. A., and B. N. Meissner (2009), The 24 February 2007 North Texas dust storm: An impact weather event, *Natl. Wea. Dig.*, *33*, 165–184.
- Skamarock, W. C., J. B. Klemp, J. Dudhia, D. O. Gill, D. M. Barker, M. G. Duda, X.-Y. Huang, W. Wang, and J. G. Powers (2008), A Description of the Advanced Research WRF Version 3, NCAR/TN-475+STR, 113 pp.
- Thompson, G., P. R. Field, W. D. Hall, and R. M. Rasmussen (2006), A new bulk microphysics parameterization for WRF and MM5, *Seventh Weather and Research Forecasting Workshop*, National Center for Atmospheric Research, Boulder, CO, NCAR.
- Thompson, G., R. M. Rasmussen, and K. Manning (2004), Explicit forecasts of winter precipitation using an improved bulk microphysics scheme. I: Description of sensitivity analysis, *Mon. Weather Rev.*, *132*, 519–542.
- Van Tuyl, A. H., and J. A. Young (1982), Numerical simulation of nonlinear jet stream adjustment, *Mon. Weather Rev.*, *110*, 2038–2054.
- Vogelmann, J. E., S. M. Howard, L. Yang, C. R. Larson, B. K. Wylie, and J. N. Van Driel (2001), Completion of the 1990's National Land Cover Data Set for the conterminous United States, *Photogramm. Eng. Remote Sens.*, *67*, 650–662.
- Zack, J. W., and M. L. Kaplan (1987), Numerical simulations of the subsynoptic features associated with the AVE-SESAME I Case, Part I: The pre-convective environment, *Mon. Weather Rev.*, *115*, 2367–2394.
- Zhang, F., S. E. Koch, C. A. Davis, and M. L. Kaplan (2000), A survey of unbalanced flow diagnostics and their applications, *Adv. Atmos. Sci.*, *17*, 165–183.